Abstract

The use of such plastic inserts (such as Vossloh dowels [1] and other *soft* fastening solutions) in pre-stressed concrete sleepers and crossing bearers has become widespread within the UK, Europe and the rest of the world. This paper uses a bespoke finite-element analysis tool [2] to, for the first time, investigate the stress state around these plastic inclusions specifically focusing on the likelihood of discontinuity development. Most continuum stress analysis methods are over simplistic, in that they assume that fracture occurs in a direction normal to the major (most tensile) principal stress once it exceeds some limiting threshold. However, simply using a limiting stress approach fails to interpret the problem from the viewpoint of material instability analysis. A more physically realistic approach requires examination of the inelastic material stiffness, to determine the direction in which the initial fractures will propagate. This rigorous continuum-discontinuum approach [3], combined with an efficient instability search algorithm, is used in this paper.

Keywords: stress analysis, fastening solutions, pre-stressed concrete, sleepers, bearers, finite-element analysis, acoustic tensor analysis, material instability.

1 Introduction

The UKs rail infrastructure currently supports 1.3 billion passenger journeys and 100 million tonnes of freight each year. The freight transport alone contributes £870 million to the UK economy [4]. The vast majority of this 32,000km of rail infrastructure is supported by pre-stressed concrete sleepers (PCSs) and crossing bearers (CBs). These concrete members provide lateral restraint and vertical support to the running steel rails. The PCSs and CBs are in turn supported on three sides by track ballast; crushed stone 30-50mm in diameter. Since their introduction in the 1950s, PCSs have

superseded traditional wooden sleepers in new track and Network Rail (NR) replaces approximately 200,000 timber sleepers each year with PCSs. However, despite the reliance of the UKs rail network on these concrete structures, and the simplicity of their geometry, surprisingly their structural behaviour is poorly understood.

PCSs are attached to the running-rail (and other components, such as the electrified third rail) through cast-in-place inclusions. Two types commonly used are: steel shoulders, designed to clamp the rail through a reaction spring, and threaded plastic inserts to allow *in-situ* bolting of components. The plastic inserts are soft relative to the surrounding concrete (10-40 times lower Youngs moduli) and create local stress concentrations exaggerated by high longitudinal pre-stressing. These concentrations have the potential to initiate longitudinal fractures that can significantly reduce the support system's designed 50-year service life. In order to maintain a safe, reliable and resilient rail network it is essential to understand how the concrete support systems can be designed to future proof them against ever increasing structural demands.

This paper describes a numerical framework that can be used to assess any potential material instabilities that arise around cast-in-place inclusions within a concrete body. In particular the numerical analyses presented in this paper focus on a plastic socket, similar to the Vossloh dowel fastening solution [1], subjected to pre-stressing loads and quantify the point at which material instabilities first arise. The difference between the continuum-discontinuum approach [3] and a simpler limiting maximum tensile stress is also explored.

The layout of this paper is as follows. Section 2 will present a simple perfect plasticity concrete model that will be used within the instability assessment framework presented in Section 3. Section 4 provides the results of a detailed finite-element analysis of a plastic socket embedded in pre-stress concrete body. Finally brief conclusions are drawn in Section 5.

2 Concrete failure criteria

This paper uses a relatively simple constitutive model for the behaviour of the concrete cast within the framework of small-strain perfect plasticity theory. Within this framework the strain, $\{\varepsilon\}$, is additively decomposed into elastic and plastic components

$$\{\varepsilon\} = \{\varepsilon^{\mathrm{e}}\} + \{\varepsilon^{\mathrm{p}}\}, \tag{1}$$

where $\{\varepsilon^{\mathrm{e}}\}$ and $\{\varepsilon^{\mathrm{p}}\}$ are the elastic and plastic strain components respectively. A linear relationship is assumed between the elastic strain and Cauchy stress vectors

$$\{\sigma\} = [D^{\mathrm{e}}]\{\varepsilon^{\mathrm{e}}\}, \tag{2}$$

where $[D^{\mathrm{e}}]$ is the elastic stiffness matrix.

The yield envelope comprises of three planar surfaces in principal stress space: (i) a Mohr-Coulomb (M-C) plane in the compressive region, (ii) a Rankine (R) cut-off in

limiting the allowable tensile stress and (iii) an additional M-C surface linking the two regions. The compressive portion of the Mohr-Coulomb (M-C) yield surface is given by

$$f_c = k\sigma_1 - \sigma_3 + \sigma_c = 0, \tag{3}$$

where $k = (1 + \sin\phi)/(1 - \sin\phi)$, σ_c is the uniaxial compressive strength of the concrete and ϕ is the effective friction angle. σ_1 and σ_3 are the major and minor principal stresses with the condition that $\sigma_1 \geq \sigma_2 \geq \sigma_3$. The tensile Rankine cut-off is given defined as

$$f_r = \sigma_1 - \sigma_t = 0, \tag{4}$$

where σ_t is the tensile strength of the concrete. These two yield surfaces are connected by an additional Mohr-Coulomb yield envelope

$$f_t = k_t\sigma_1 - \sigma_3 + \sigma_c = 0 \tag{5}$$

where $k_t = |\sigma_c/\sigma_t|$. The combined yield surface

$$f = \max(f_c,\ f_r,\ f_t) = 0 \tag{6}$$

is shown in σ_1 versus σ_3 biaxial, and principal stress spaces in Figure 1.

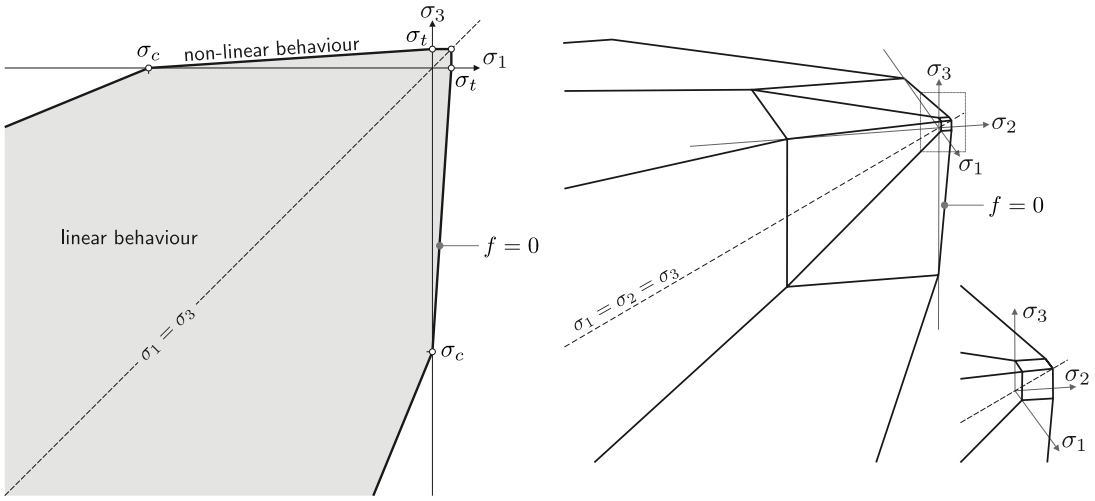

Figure 1: Non-linear concrete model in: (a) biaxial stress space (linear grey area and non-linear thick black line) and (b) principal stress space.

The plastic strains evolve according to

$$\{\dot{\varepsilon}^{\mathrm{p}}\} = \dot{\gamma}\{g_{,\sigma}\}, \tag{7}$$

where $\dot{\gamma}$ is the scalar plastic multiplier and $\{g_{,\sigma}\}$ is the plastic flow direction (the derivative of the plastic potential with respect to stress). The principal flow directions

for the three surfaces are

$$\{g^c_\sigma\} = \left\{ \begin{array}{c} m \\ 0 \\ -1 \end{array} \right\} \qquad \{g^t_\sigma\} = \left\{ \begin{array}{c} m_t \\ 0 \\ -1 \end{array} \right\} \quad \text{and} \quad \{g^r_\sigma\} = \left\{ \begin{array}{c} 1 \\ 0 \\ 0 \end{array} \right\}, \tag{8}$$

where $m = (1 + \sin\psi)/(1 - \sin\psi)$ and $m_t = (1 + \sin\psi_t)/(1 - \sin\psi_t)$ where ψ and ψ_t are the dilation angles for the two planar surfaces. (7) is subject to the standard Kuhn-Tucker-Karush consistency conditions

$$f(\sigma_i) \leq 0, \qquad \dot{\gamma} \geq 0 \qquad \text{and} \qquad f(\sigma_i)\dot{\gamma} = 0. \tag{9}$$

These conditions enforce that the material must either be on the yield surface undergoing elasto-plastic deformation ($f = 0$ and $\dot{\gamma} \geq 0$) or inside the yield surface with purely elastic behaviour ($f \leq 0$ and $\dot{\gamma} = 0$).

2.1 Stress integration

The central problem in computational plasticity is given a previously converged elastic strain state, $(\varepsilon^{\mathrm{e}}_n)_i$ (or equivalently a converged stress state, σ^n_i), that is subjected to a strain increment, $\Delta\varepsilon_i$, what is the updated elastic strain state, $(\varepsilon^{\mathrm{e}}_{n+1})$? The strain increment comes from the boundary value simulation under consideration. The problem stems from the fact that inelastic constitutive relationships are constructed in rate form and must be integrated to create such an incremental relationship.

Note that all of the yield surfaces presented in this paper are isotropic and therefore the stress return algorithm can be constructed in principal stress space. This does not detract from the generality of the algorithm as the generalised six-component stress and strain measures are simply converted to principal stress space and back again at the input and output of the function. See [5], amongst many others, for more details.

In this paper we consider elastic predictor, plastic corrector schemes. Within this framework the elastic trial strain is given by

$$\{\sigma_{tr}\} = \{\sigma_n\} + \{\Delta\sigma\}, \qquad \text{where} \qquad \{\Delta\sigma\} = [D^{\mathrm{e}}]\{\Delta\varepsilon\} \tag{10}$$

and

$$\{\sigma_n\} = [D^{\mathrm{e}}]\{\varepsilon^{\mathrm{e}}_n\}. \tag{11}$$

$\{\sigma_n\}$ and $\{\varepsilon^{\mathrm{e}}_n\}$ are the stress and elastic strain states from the previous load (or time) step in the global solution algorithm, $\{\Delta\varepsilon\}$ is the strain increment from associated with the global boundary value displacement

If the trial elastic stress state, $\{\sigma_t\}$, exceeds the yield envelope ($f > 0$) then it must be corrected back onto the yield surface using a plastic stress increment

$$\{\sigma_{n+1}\} = \{\sigma_{tr}\} - \{\Delta\sigma^{\mathrm{p}}\}, \qquad \text{where} \qquad \{\Delta\sigma^{\mathrm{p}}\} = [D^{\mathrm{e}}]\{\Delta\varepsilon^{\mathrm{p}}\} \tag{12}$$

ID	description	return type
A	Rankine apex, f_r	point
B	compression meridian intersection of f_t and f_r	point
C	extension meridian intersection of f_t and f_r	point
D	Rankine compression meridian, f_r	line
E	intersection of the transition M-C and R planes, f_t and f_r	line
F	Rankine plane, f_r	plane
G	compression meridian of f_t	line
H	extension meridian of f_t	line
I	M-C transition plane, f_t	plane
J	intersection of the two M-C planes, f_c and f_t	line
K	compression meridian intersection of f_t and f_c	point
L	extension meridian intersection of f_t and f_c	point
M	compression meridian of the M-C plane, f_c	line
N	extension meridian of the M-C plane, f_c	line
P	main M-C plane, f_c	plane

Table 1: Stress return regions for the combined yield surface.

and $\Delta\epsilon_j^{\mathrm{p}}$ is the plastic strain increment obtained from the incremental form of (7). Once this correction has been applied the updated elastic strain can be obtained from

$$\{\varepsilon_{n+1}^{\mathrm{e}}\} = \{\varepsilon_n^{\mathrm{e}}\} + \{\Delta\varepsilon\} - \{\Delta\varepsilon^{\mathrm{p}}\}. \tag{13}$$

This paper follows the approach of Clausen *et al.* [6, 7] to construct analytical stress return solutions for the 15 return locations give in Table 1. Depending on the return type (point, line or plane), the return procedure is different as is the material stiffness tangent used in the global boundary value simulation (see [6, 7] for full details).

2.2 Material tangents

To achieve optimal convergence within a boundary value simulation it is essential to linearise the stress integration algorithm to form the algorithmic consistent tangent (that is, the fourth order material stiffness tensor that is consistent with the stress-strain algorithm). This paper again uses the approach of Clausen *et al.* [6, 7] to construct the algorithmic consistent tangent. It is this tangent that is used by the finite-element program to determine the stiffness of each element in the analysis allowing asymptotic quadratic convergence of the global error.

The material instability analysis presented in Section 3 requires the formation of the infinitesimal elasto-plastic stiffness tangent, $[D^{\mathrm{ep}}]$. This tangent links an infinitesimal change of stress with total strain, that is

$$\{\dot{\sigma}\} = [D^{\mathrm{ep}}]\{\dot{\varepsilon}\}. \tag{14}$$

For the planar surface returns the tangent is given by

$$[D^{\text{ep}}] = \big[D^{\text{e}}\big] \overbrace{\left[[I] - \frac{\{g_{,\sigma}\}\{f_{,\sigma}\}^T\big[D^{\text{e}}\big]}{\{f_{,\sigma}\}^T\big[D^{\text{e}}\big]\{g_{,\sigma}\}}\right]}^{\text{rank-one update of } [D^{\text{e}}]}, \tag{15}$$

where $\{f_{,\sigma}\}$ is the derivative of the yield surface with respect to stress and $[I]$ is the identity matrix. The elasto-plastic tangent for other return locations are given by [6, 7], in the subsequent section this tangent is used to definite the point at which continuum assumptions are no longer valid.

3 Acoustic tensor analysis

Since the 1958 and 1962 papers by Hill [3, 8], there has been a strong interest in the mathematical identification of instabilities which can be predicted purely from the characteristics of the constitutive equations [9–22]. Failure[1] indicators in materials can be grouped into two categories: continuous (or loss of stability) and discontinuous (or localisation) [10]. In continuous failure, the homogeneity of strains (and stresses) is preserved, whereas for discontinuous failure a spatial discontinuity is observed in the strain rate field. Continuous failure can be detected through investigating the infinitesimal elasto-plastic tangent, $[D^{\text{ep}}]$. The first indicator occurs when the determinant of the symmetric component of $[D^{\text{ep}}]$ falls to zero

$$\det\left(\frac{1}{2}\Big([D^{\text{ep}}] + [D^{\text{ep}}]^T\Big)\right) = 0. \tag{16}$$

We refer to this as a *strong* indicator of the loss of stability. The second indicator occurs when the determinant of $[D^{\text{ep}}]$ falls to zero we refer to this as a *weak* indicator of the loss of stability. These two continuous failure indicators can be expressed as

$$e_{\mathsf{A}} = \underbrace{\min\left(\frac{\det[D^{\text{ep}}_{sym}]}{\det[D^{\text{e}}]}\right)}_{\text{strong instability}} \qquad \text{and} \qquad e_{\mathsf{D}} = \underbrace{\min\left(\frac{\det[D^{\text{ep}}]}{\det[D^{\text{e}}]}\right)}_{\text{weak instability}}, \tag{17}$$

where $[(\cdot)_{sym}]$ denotes the symmetric component of $[(\cdot)]$. The first of these, e_{A}, is the stricter condition (that is, a material will fail e_{A} prior to e_{D}) than the second. This is due to the fact that the eigenvalues of the symmetric component of a positive definite tensor bound those of the full matrix. If $[D^{\text{ep}}]$ is positive definite (that is, $\det\big([D^{\text{ep}}_{sym}]\big) > 0$) then the material response is unique under any loading [20].

In a load (or equivalently stress) controlled test, we have the following relation between the rate of change of strain with stress

$$\{\dot{\varepsilon}\} = [D^{\text{ep}}]^{-1}\{\dot{\sigma}\}. \tag{18}$$

[1]Here, the term failure is used to describe when the material no longer behaves as a continuum, that is, some loss of stability or bifurcation of the material has taken place.

When the determinant of the infinitesimal elasto-plastic tangent fall to zero, $\{\dot{\varepsilon}\}$ is undefined and we obtain a loss of uniqueness of the strain solution for stress states less than the point of $\det\big([D^{\text{ep}}]\big) = 0$ [20], as shown in Figure 2. Under strain (or displacement) controlled simulations, we have an equivalent relation to that of the stress controlled test, however now

$$\{\dot{\sigma}\} = [C^{\text{ep}}]^{-1}\{\dot{\varepsilon}\}. \tag{19}$$

Here $[C^{\text{ep}}] = [D^{\text{ep}}]^{-1}$ is the infinitesimal elasto-plastic compliance matrix. A loss of uniqueness occurs when the determinant of $[C^{\text{ep}}]$ falls to zero [20], that is when

$$\{f_{,\sigma}\}^T \big[D^{\text{e}}\big]\{g_{,\sigma}\} = 0. \tag{20}$$

in a non-associated, perfect-plasticity elasto-plastic material (refer to the denominator of (15)). This condition corresponds to a *snap-back* in the stress versus strain response of the material, as shown by point E in Figure 2.

Discontinuous failure indicators grew out of the work by Hill [8] on acceleration waves. Hill considered planes (with unit normal denoted by n_i or $\{n\}$) across which the acceleration was discontinuous. This jump in acceleration is equivalent to a jump in the strain rate (and consequently the stress rate) in a material's constitutive relations [8]. Using Hill's procedure, a localisation (or acoustic) tensor can be defined as

$$(Q^{(\cdot)}_{at})_{jk} = n_i D^{(\cdot)}_{ijkl} n_l, \tag{21}$$

where $D^{(\cdot)}_{ijkl}$ is the fourth-order tangent stiffness tensor under consideration. Alternatively (21) can be expressed in matrix form using the following expression

$$\big[Q^{(\cdot)}_{at}\big] = \big[T\big]^T \big[D^{(\cdot)}\big]\big[T\big], \qquad \text{where} \qquad \big[T\big]^T = \begin{bmatrix} n_1 & 0 & 0 & 0 & n_3 & n_2 \\ 0 & n_2 & 0 & n_3 & 0 & n_1 \\ 0 & 0 & n_3 & n_2 & n_1 & 0 \end{bmatrix}, \tag{22}$$

where n_i are the components of the normal to the potential discontinuity plane. The acoustic tensor allows us to specify two indicators of localisation

$$e_{\mathsf{B}} = \underbrace{\min\left(\frac{\det[Q^{\text{ep}}_{at_{sym}}]}{\det[Q^{\text{e}}_{at}]}\right)}_{\text{strong localisation}} \qquad \text{and} \qquad e_{\mathsf{C}} = \underbrace{\min\left(\frac{\det[Q^{\text{ep}}_{at}]}{\det[Q^{\text{e}}_{at}]}\right)}_{\text{weak localisation}}, \tag{23}$$

where $[Q^{\text{ep}}_{at}]$ and $[Q^{\text{e}}_{at}]$ denote the acoustic tensors associated with $[D^{\text{ep}}]$ and $[D^{\text{e}}]$ using the same search direction n_i. For the case of associated plasticity, $[D^{\text{ep}}]$ is symmetric and the localisation indicators e_{B} and e_{C} are identical, as are e_{A} and e_{D}.

The Bromwich bounds [24] allows the sequence of failure indicators to be established. e_{A} is the strictest condition, followed by e_{B}, then e_{C} and finally e_{D} [25]; shown schematically in Figure 2. The determinant of $[C^{\text{ep}}]$ drops to zero at point E in Figure 2 after passing through the non-unique stress point.

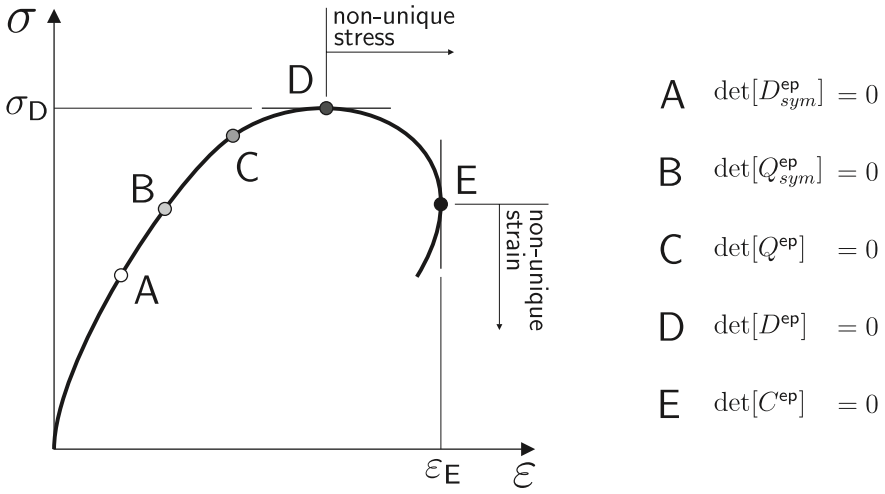

Figure 2: Hierarchy of failure indicators (reproduced with permission from [23]).

3.1 Search algorithm

Acoustic tensor analysis requires the determination of the normal direction corresponding to the minimum determinant of the acoustic tensor, $[Q^{\text{ep}}_{at}]$. Note that it is necessary to only search one hemisphere of normal directions rather than the complete sphere of possible directions. Here an efficient search algorithm is adopted that initially equally spaces a number of search directions over this hemisphere using the HEALpix algorithm of Górski et al. [26]. From this initial search cloud, the point with the lowest value of the determinant of the acoustic tensor is taken as the starting point for a Newton-Raphson search algorithm similar to that used by Andrade and Borja [22].

4 Numerical computations

This section presents the finite-element analysis of a cast-in-place plastic socket subjected to longitudinal pre-stress. Only a local region of concrete surrounding the socket was modelled using 20-noded fully-integrated hexahedral elements (tri-quadratic element with 27 Gauss points arranged in a 3 by 3 by 3 grid). The material constants for the concrete constitutive model, as described in Section 2, are given in Table 2. The plastic socket modelled as an isotropic linear elastic material with a Young's modulus of 1.1GPa and a Poisson's ratio of 0.2. The finite-element analyses were conducted using a bespoke finite-element code developed at Durham University based on the finite deformation elasto-plastic code of Coombs et al. [2], however in this paper only small strain elasto-plastic simulations are undertaken.

The volume of concrete modelled had a height of 165mm and a width and breadth of 250mm; typical sleepers and bearers have cross sections ranging between 140-205mm in height and 250-380mm in width and are typically subjected to an average

material constant	E	ν	σ_c	σ_t	ϕ	ψ	ψ_t
value	45GPa	0.2	-40MPa	$-\sigma_c/15$	37°	0°	0°

Table 2: Concrete material constants for the numerical analysis (representative values at the point of transfer of the pre-stressing loads).

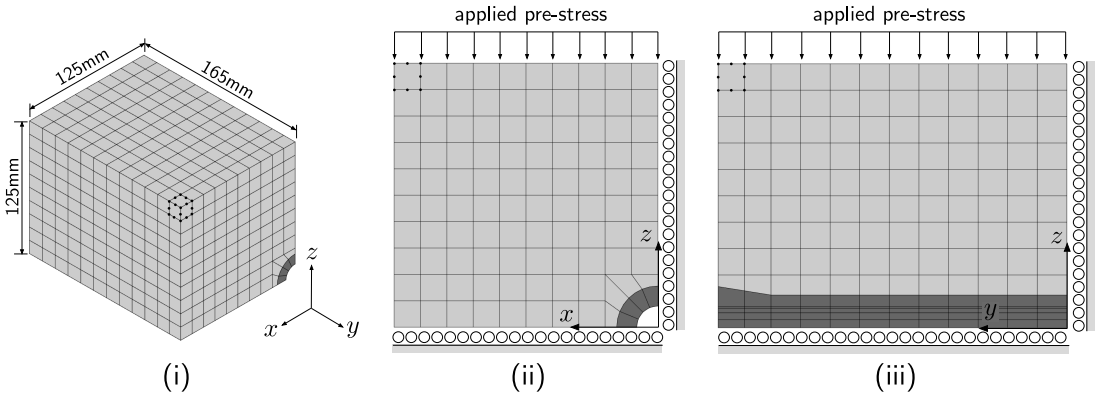

Figure 3: Finite-element discretisation using 20-noded hexaherdal elements: (i) three-dimensional view of the mesh, (ii) plan view and (iii) side elevation looking in the positive x-direction. The light and dark shaded elements are concrete and plastic, respectively. The circles on parts (ii) and (iii) indicate roller boundary conditions.

compressive longitudinal pre-stress of between 11 and 15MPa. Here the analysis applied a compressive longitudinal stress of 11MPa over 100 loadsteps. Due to symmetry only one quarter of the problem was analysed, as shown in Figure 3. The central plastic socket was modelled having a total length of 165mm, a uniform internal diameter of 20mm and an external diameter of 39mm at the top surface of the mesh, tapering to a diameter of 31mm over 25mm down the length of the socket. Full displacement compatibility was assumed between the concrete and plastic elements and only pre-stressing loads are considered.

The evolution of the minimum determinant of the acoustic tensor (solid grey line) and the number of elasto-plastic points (dashed line) with applied pre-stress is shown in Figure 4 and four key points have been identified. The onset of elasto-plasticity occurs at an applied pre-stress of 3.1MPa and at this point (point B on Figure 4) there was a dramatic reduction in the minimum determinant of the normalised acoustic tensor, e_{C}. Up to this point e_{C} is equal to one as the elasto-plastic stiffness is equal to the elastic stiffness matrix.

At point C in Figure 4 the all of the instability indicators drop below zero, the values of these indicators (e_{A} through e_{D}) are given Table 3. It is at this point that the analysis suggests that some loss of stability or bifurcation of the material has taken place. As the pre-stress increases the global minimum of e_{C} continues to reduce however, the instability analysis only allows a binary interpretation of the indicators - that is continuum or discontinuum.

The curious surface plots in Figures 4 illustrate a way of visualising the determinant

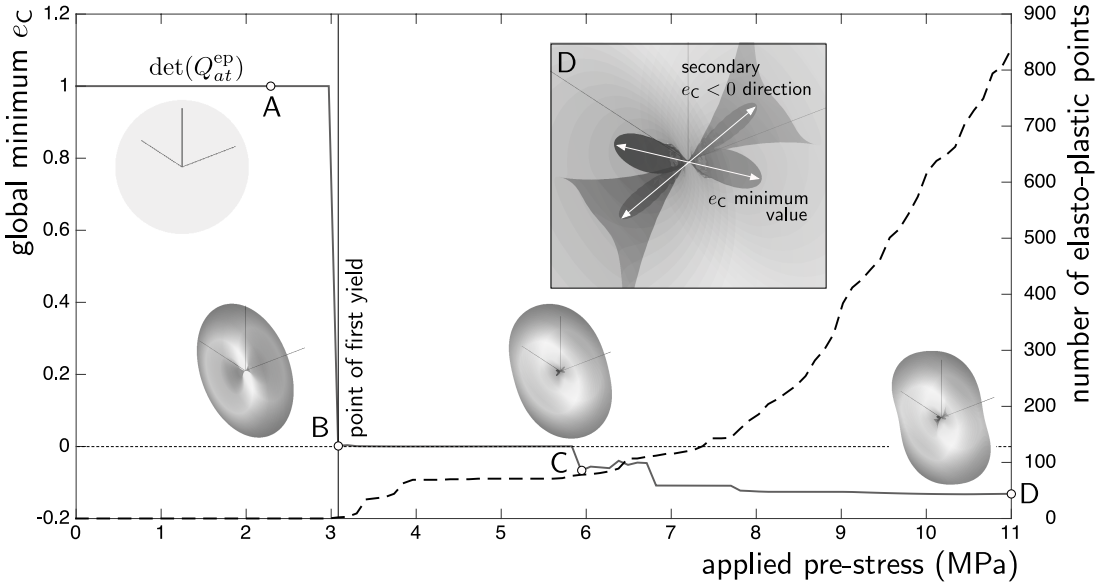

Figure 4: Evolution of the minimum determinant of the acoustic tensor (solid grey line) and the number of elasto-plastic points (dashed line) with applied pre-stress. The inset figures show the acoustic tensor surfaces at four points during the analysis.

point	A	B	C	D
e_A	1.00×10^{00}	7.43×10^{-20}	-3.19×10^{-01}	-3.19×10^{-01}
e_B	1.00×10^{00}	2.09×10^{-03}	-2.56×10^{-01}	-2.90×10^{-01}
e_C	1.00×10^{00}	2.09×10^{-03}	-6.70×10^{-02}	-1.31×10^{-01}
e_D	1.00×10^{00}	7.43×10^{-20}	-7.09×10^{-17}	-2.70×10^{-16}

Table 3: Concrete material constants for the numerical analysis (representative values at the point of transfer of the pre-stressing loads).

of the acoustic tensor. The HEALPix software [26], which divides the surface of a sphere into equal area patches, was used to generate 10,800 normal directions, $\{n\}$, for the acoustic tensor analysis (in this case over the entire sphere rather than just a hemisphere to aim visualisation). For each of the 10,800 search directions, the determinant of the acoustic tensor is calculated and a point generated from

$$\{x\} = \frac{\det\left([Q^{ep}_{at}]\right)}{\det\left([Q^{e}_{at}]\right)}\{n\} = e_C\{n\}. \tag{24}$$

A surface is then constructed through these points. If the determinate of the acoustic tensor drops to zero then the surface will pass through the origin whereas for a purely elastic material the surface will be a unit sphere. This is a useful visual indicator of the reduction in the determinant of the acoustic tensor with respect to various search directions rather than just a single minimum value. These surfaces have been plotted for points A through D (see Figure 4) for the Gauss point in the simulation that has the minimum e_C in the analysis. At A the acoustic tensor surface is a unit sphere due

to the elastic behaviour however at the onset of elaso-plastic behaviour (point B) the minimum determinant of the acoustic tensor surface drops to almost zero with the normal direction of minimum determinant closely aligned with the x-axis. At point C the e_{C} instability indicator drops below zero with two directions of instability apparent from the inset surface. This is more visible at point D, particularly in the enlarged view of the acoustic tensor surface where the two instability directions have been identified.

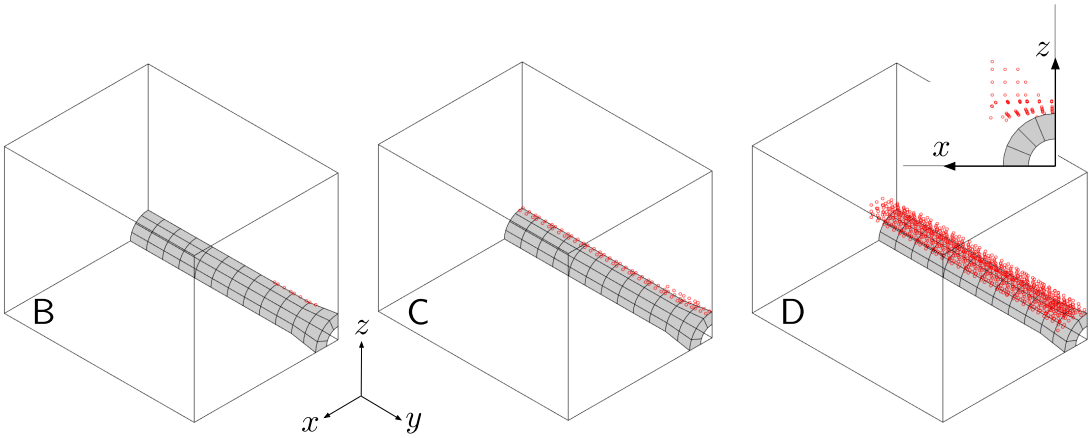

Figure 5: Elasto-plastic points at three points during the analysis (see Figure 4), a top plan view is also shown for point D.

The elasto-plastic Gauss quadrature locations for points B, C and D are shown in Figure 5. At the point of first yield (point B) the elasto-plastic points are located at the longitudinal limit of the plastic socket in the region immediately below the tapered section of the insert. By point C at approximately 6MPa of pre-stress the extent of elasto-plasticity spans the full depth of the concrete section with a larger region of elasto-plasticity beginning to develop below the tapered part of the plastic socket. At the end of the analysis (point D and a pre-stress of 11MPa) a plastic region approximately equal in size to the outer radius of the socket has developed, this is clearly seen by the inset plan view.

Figure 6 shows three predictions of the instability normal directions at the end of the analysis based on: (i) major (most tensile) principal stress for points that exceed the yield criterion, (ii) major plastic strain and (iii) the minimum value of e_{C}. Note that any fracture planes will develop perpendicular to these normal directions. Both the major principal stress and major plastic strain vectors have been scaled according to their magnitude. It is clear that both the locations and directions of the instabilities differ for the three methods, the most noticeable difference being between the acoustic tensor analysis and the other methods. The acoustic tensor analysis predicts two dominant directions, consistent with the two negative e_{C} directions shown in Figure 4.

Following the procedure of Borja and Aydin [27], comparing the search direction, $\{n\}$, with the eigenvector associated with the minimum eigenvalue of $[Q_{at}^{\text{ep}}]$ (denoted

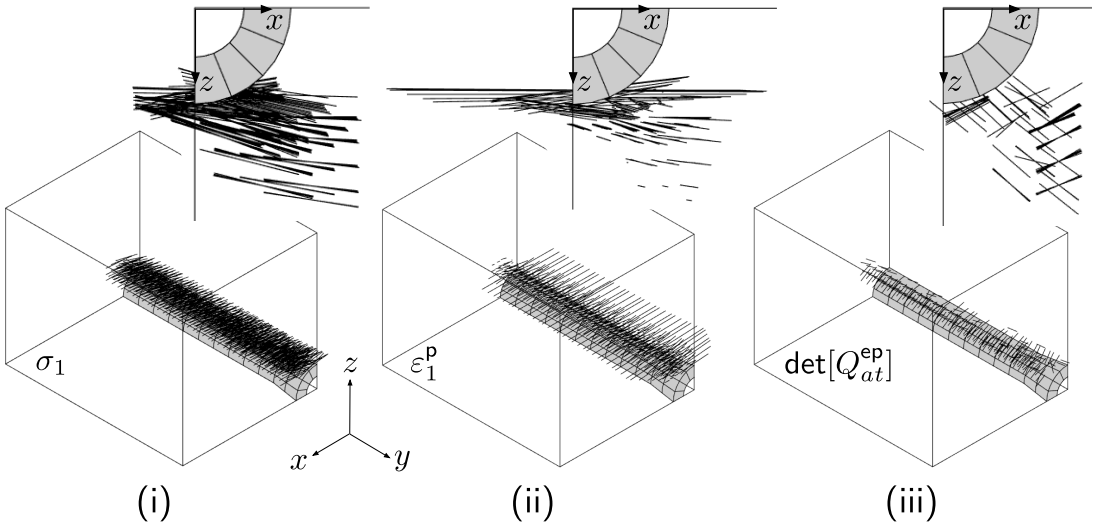

Figure 6: Potential discontinuity plane normal directions based on: (i) major principal stress, (ii) major plastic strain and (iii) the minimum determinant of the acoustic tensor. The inset figures show top plan views for the three cases.

here by $\{v_{\min}\}$), we can determine the mode of the discontinuity,as follows

$$\text{mode} = \{n\}^T\{v_{\min}\} : \begin{array}{ll} = -1 & \text{pure compaction} \\ < 0 & \text{compactive shear} \\ = 0 & \text{simple shear } (\equiv \text{fracture mode II or III}) \\ > 0 & \text{dilative shear} \\ = 1 & \text{pure dilation } (\equiv \text{fracture mode I}) \end{array} \tag{25}$$

The direction of the eigenvector associated with the minimum eigenvalue, $\{v_{\min}\}$, can be positive or negative. The direction of $\{v_{\min}\}$ can be determined from the requirement that [27]

$$\{f_{,\sigma}\}^T[D^{\mathrm{e}}]\{\xi\} > 0, \qquad \text{where} \qquad [\xi] = \{v_{\min}\}\{n\}^T. \tag{26}$$

$\{\xi\}$ is the instability *characteristic* vector, whose trace is equivalent to the mode defined in (25) (that is, $\text{tr}[\xi] = \{v_{\min}\}^T\{n\}$), where $\{\xi\}$ is the vector equivalent of $[\xi]$. The inequality in (26) stems from the assumption that the material is exhibiting some inelastic behaviour on both sides of the instability plane.

From (25) and (26) for point D the minimum e_{C} corresponded to a mode of 0.217, that is a dilative shear band. This is consistent between points C and D in the analysis and it is not possible to obtain this information from by considering the major principal stress or plastic strain directions alone.

5 Conclusion

A rigorous continuum-discontinuum approach [3], combined with an efficient instability search algorithm, was used in this paper to assess potential discontinuities that

develop around plastic sockets embedded in pre-stresses concrete. The analysis considered a plastic dowel with a geometry typical of those used to attach components to pre-stressed concrete sleepers and crossing bearers. It was observed that instabilities first manifest themselves at a pre-stress of approximately 6MPa once an elasto-plastic zone has developed through the full depth of the concrete. This discontinuity appears to behave as a dilative shear band starting from the surface of the plastic socket. A noticeable difference was observed between the directions predicted by the acoustic tensor analysis and those obtained from the major (most tensile) principal stress and plastic strain directions.

Based on the analyses presented in this paper, the use of plastic inserts within pre-stressed concrete components increases the potential for longitudinal fracture development.

Acknowledgements

The author acknowledges the support of the Engineering and Physical Sciences Research Council (EPSRC) grant no. EP/M017494/1.

References

[1] Vossloh fastening systems. URL `www.vossloh-fastening-systems.com`. accessed on 1st June 2015.

[2] W M Coombs, R S Crouch, and C E Augarde. 70-line 3d finite deformation elastoplastic finite-element code. In T Benz and S Nordalm, editors, *7th European Conference on Numerical Methods in Geoetchnical Engineering (NUMGE)*, pages 151–156, Trondheim, Norway, June 2010.

[3] R. Hill. A general theory of uniqueness and stability in elastic-plastic solids. *Journal of the Mechanics and Physics of Solids*, 6(3):236 – 249, 1958. ISSN 0022-5096.

[4] Britain relies on rail. URL `www.networkrail.co.uk/aspx/662.aspx`. accessed on 1st June 2015.

[5] W M Coombs, R S Crouch, and C E Augarde. Reuleaux plasticity: analytical backward Euler stress integration and consistent tangent. *Comput. Methods Appl. Mech. Engrg.*, 199:1733–1743, 2010. doi: doi:10.1016/j.cma.2010.01.017.

[6] J Clausen, L Damkilde, and L Andersen. Efficient return algorithms for associated plasticity with multiple yield planes. *Int. J. Numer. Meth. Engng*, 66: 1036–1059, 2006.

[7] J Clausen, L Damkilde, and L Andersen. An efficient return algorithm for non-associated plasticity with linear yield criteria in principal stress space. *Computers & Structures*, 85:1795–1807, 2007.

[8] R Hill. Acceleration waves in solids. *J. Mech. Phys. Solids*, 10:1–16, 1962.

[9] K.J. Willam and E.P. Warnke. Constitutive model for the triaxial behaviour of concrete. In *Proceedings of the May 17-19 1974, International Association of Bridge and Structural Engineers Seminar on Concrete Structures Subjected to Triaxial Stresses, held at Bergamo Italy*, 1974.

[10] E Rizzi, G Maier, and K Willam. failure indicators in multi-dissipative materials. *Int. J. Solids Structures*, 33:3187–3214, 1996.

[11] D Bigoni and T Hueckel. Uniqueness and localizationi. associative and non-associative elastoplasticity. *Int. J. Solids Structures*, 28:197–213, 1991.

[12] D Bigoni and T Hueckel. Uniqueness and localizationii. coupled elastoplasticity. *Int. J. Solids Structures*, 28:215–224, 1991.

[13] J Mosler. Numerical analyses of discontinuous material bifurcation: strong and weak discontinuities. *Computer Methods in Applied Mechanics and Engineering*, 194:979–1000, 2005.

[14] D Bigoni and D Zaccaria. On the eigenvalues of the acoustic tensor in elastoplasticity. *Eur. J. Mech. A/Solids*, 13:621–638, 1994.

[15] D Bigoni. Bifurcation and instability of non-associative elastoplastic solids. In *Material instabilities in elastic and plastic solids*, pages 1–52. Springer-Verlag, Wien New York, 2000.

[16] R. I. Borja. Cam-clay plasticity. part v: A mathematical framework for three-phase deformation and strain localization analyses of partially saturated porous media. *Comput. Methods Appl. Mech. Eng.*, 193:5301–5338, 2004.

[17] J Oliver, AE Huespe, JC Canta, and G Díaz. On the numerical resolution of the discontinuous material bifurcation problem. *Int. J. Numer. Meth. Engng*, 93: 786–804, 2010.

[18] HL Schreyer and MK Neilsen. Discontinuous bifurcation states for associated smooth plasticity and damage with isotropic elasticity. *Int. J. Solids Structures*, 33:3239–3256, 1996.

[19] L Xue and T Belytschko. Fast methods for determining instabilities of elastic-plastic damage models through closed-form expressions. *Int. J. Numer. Meth. Engng*, 84:1490–1518, 2010.

[20] S Imposimato and R Nova. An investigation on the uniqueness of the incremental response of elastoplastic models for virgin sand. *MECHANICS OF COHESIVE-FRICTIONAL MATERIALS*, 3:65–87, 1998.

[21] JW Rudnicki and JR Rice. Conditions for the localization of deformation in pressure-sensitive dilatant materials. *J. Mech. Phys. Solids*, 23:371–394, 1975.

[22] J E Andrade and R I Borja. Capturing strain localization in dense sands with random density. *Int. J. Numer. Meth. Engng*, 67:1531–1564, 2006.

[23] W.M. Coombs. *Finite deformation of particulate geomaterials: frictional and anisotropic Critical State elasto-plasticity*. PhD thesis, Durham University, 2011.

[24] T. J. Bromwich. Quadratic forms and their classification by means of invariant factors. *Cambridge Tracts in Mathematics and Mathematical Physics*, 1906.

[25] KJ Willam and M-M Iordache. On the lack of symmetry in materials. In WA Wall, K-U Bletzinger, and K Schweizerhof, editors, *Trends in computational structural mechanics*, 2001.

[26] KM Górski, E Hivon, AJ Banday, BD Wandelt, FK Hansen, M Reinecke, and M Bartelmann. Healpix: A framework for high-resolution discretization and fast analysis of data distributed on the sphere. *The Astrophysical Journal*, 622: 759–771, 2005.

[27] R. I. Borja and A Aydin. Computational modeling of deformation bands in granular media. i. geological and mathematical framework. *Comput. Methods Appl. Mech. Engrg.*, 193:2667–2698, 2004.